Direct and compound-nucleus reaction mechanisms in the ^{7}Be + ^{58}Ni system at near-barrier energies

M. Mazzocco,[1,2,*] D. Torresi,[1,2,†] D. Pierroutsakou,[3] N. Keeley,[4] L. Acosta,[5,6,‡] A. Boiano,[3] C. Boiano,[7] T. Glodariu,[8] A. Guglielmetti,[9,7] M. La Commara,[10,3] J. A. Lay,[1,2] I. Martel,[5] C. Mazzocchi,[9,7,§] P. Molini,[1,2,‖] C. Parascandolo,[3] A. Pakou,[11] V. V. Parkar,[5,¶] M. Romoli,[3] K. Rusek,[12] A. M. Sánchez-Benítez,[5,#] M. Sandoli,[10,3] O. Sgouros,[11] C. Signorini,[1,2,**] R. Silvestri,[10,3] F. Soramel,[1,2] V. Soukeras,[11] E. Stiliaris,[13] E. Strano,[1,2] L. Stroe,[8] and K. Zerva[11]

[1]*Dipartimento di Fisica e Astronomia, Università di Padova, via F. Marzolo 8, I-35131 Padova, Italy*

[2]*INFN-Sezione di Padova, via F. Marzolo 8, I-35131 Padova, Italy*

[3]*INFN-Sezione di Napoli, via Cintia, I-80126 Napoli, Italy*

[4]*National Centre for Nuclear Research, ulica Andrzeja Sołtana 7, 05-400 Otwock, Poland*

[5]*Departamento de Fìsica Aplicada, Universidad de Huelva, Campus de El Carmen, E-21071 Huelva, Spain*

[6]*INFN-Sezione di Catania, via Santa Sofia 64, I-95123 Catania, Italy*

[7]*INFN-Sezione di Milano, via Celoria 16, I-20133 Napoli, Italy*

[8]*NIPNE, 30 Reactorului Street, 077125 Magurele, Romania*

[9]*Dipartimento di Fisica, Università di Milano, via Celoria 16, I-20133 Padova, Italy*

[10]*Dipartimento di Fisica, Università di Napoli "Federico II", via Cintia, I-80126 Napoli, Italy*

[11]*Department of Physics and HINP, University of Ioannina, 45110 Ioannina, Greece*

[12]*Heavy Ion Laboratory, University of Warsaw, ulica Pasteura 5a, 02-093 Warsaw, Poland*

[13]*Institute of Accelerating Systems and Applications and Department of Physics, University of Athens, Athens, Greece*

(Received 22 July 2015; published 20 August 2015)

The energy and angular distributions of ^{3}He and ^{4}He ions produced in the ^{7}Be + ^{58}Ni reaction at a bombarding energy of 22 MeV have been measured for the first time. The yield of the heavier helium isotope was four to five times more abundant than that of its lighter counterpart, ruling out the possibility that in this energy range the ^{7}Be reaction dynamics is dominated by the exclusive breakup process $^{7}\mathrm{Be} \rightarrow {}^{3}\mathrm{He} + {}^{4}\mathrm{He}$ ($S_{\alpha} = 1.586$ MeV). Extensive kinematic and theoretical calculations suggest that the ^{3}He ions mostly originate from the ^{4}He-stripping process and the ^{4}He production is mainly triggered by the fusion-evaporation channel. The role played by the breakup, ^{3}He-stripping, 1n-stripping, and 1n-pickup processes is also discussed.

DOI: 10.1103/PhysRevC.92.024615 PACS number(s): 24.10.Eq, 25.60.Bx, 25.60.Je, 25.60.Pj

I. INTRODUCTION

The study of the reaction dynamics of light weakly bound radioactive ion beams (RIBs) is currently an active research field in nuclear physics. The scenario is particularly intriguing when the bombarding energy approaches the Coulomb barrier, since the exotic features of light RIBs may lead to competing effects. Many light RIBs present nuclear matter distributions that can be described by a (mostly) inert core surrounded by a halo of rarefied nuclear matter (halo nuclei, e.g., ^{6}He, ^{11}Li, and ^{11}Be). Other light radioactive nuclei are characterized by larger than usual neutron densities in the proximity of the nuclear surface (neutron skin nuclei, e.g., ^{8}He, ^{14}Be, and ^{19}B). Moreover, as a quite general feature, light RIBs are typically very weakly bound with particle emission thresholds lower than 1 MeV and with well pronounced cluster structures in their ground states. All these phenomena are strongly interconnected and usually increase the variety of reaction mechanisms in nuclear collisions at near-barrier energies. Several review articles have recently been written on this topic [1–6].

In particular, a large enhancement of the total reaction cross section [7–9] has been observed for reactions induced by halo nuclei on medium-mass and heavy targets. The focus has now moved towards investigating which reaction channels are mostly responsible for this enhancement. These studies are still very challenging owing to the limited intensity of currently available RIBs.

Experiments carried out so far indicate neutron transfer channels as the main mechanism for the enhancement of the total reaction cross section in reactions induced by the 2n-halo nucleus ^{6}He (see, for instance, [10–18]) and the neutron skin nucleus ^{8}He [19,20]. On the other hand, more recent studies for the p halo ^{8}B [21,22] and the 2n halo ^{11}Li [23,24] suggest that, in these cases, the enhancement might be mainly due to the projectile breakup process.

*marco.mazzocco@pd.infn.it

†Present address: Dipartimento di Fisica e Astronomia, Università di Catania, via Santa Sofia 64, I-95123 Catania, Italy.

‡Present address: Instituto de Fìsica, Universidad Nacional Autonoma de Mexico, Apartado Postal 20-364, Mexico D. F. 01000, Mexico.

§Present address: Institute of Experimental Physics, University of Warsaw, ul. Pasteura 5, 02-093 Warsaw, Poland.

‖Present address: Fondazione Bruno Kessler, Scientific and Technology Hub, via Sommarive 18, I-38123 Povo (TN), Italy.

¶Present address: Nuclear Physics Division, Bhabha Atomic Research Centre, Mumbai 400085, India.

#Present address: Nuclear Physics Center, University of Lisbon, Avda. Prof. Gama Pinto 2, 1649-003 Lisbon, Portugal.

**Present address: INFN-LNL, viale dell'Università 2, I-35020 Legnaro (PD), Italy.

Within this framework and with the aim of shedding more light on the interplay between different reaction mechanisms at Coulomb barrier energies, we undertook a study of the nuclear reactions of the ^{7}Be + ^{58}Ni system at a bombarding energy of 22 MeV.

The ^{7}Be nucleus is radioactive with a well pronounced ^{3}He + ^{4}He cluster structure and is bound by only 1.586 MeV with respect to ^{7}Be $\rightarrow$ ^{3}He + ^{4}He breakup. From an experimental point of view all the most relevant direct processes induced by ^{7}Be, viz. ^{7}Be $\rightarrow$ ^{3}He + ^{4}He breakup, ^{7}Be + ^{58}Ni $\rightarrow$ ^{6}Be (^{4}He + p + p) + ^{59}Ni 1n stripping, ^{7}Be + ^{58}Ni $\rightarrow$ ^{8}Be (^{4}He + ^{4}He) + ^{57}Ni 1n pickup, ^{7}Be + ^{58}Ni $\rightarrow$ ^{4}He + ^{61}Zn ^{3}He stripping, and ^{7}Be + ^{58}Ni $\rightarrow$ ^{3}He + ^{62}Zn ^{4}He stripping, produce either one or two stable well-bound charged fragments. Thus, in contrast to reactions induced by other light nuclei, studies of ^{7}Be reaction dynamics do not require the detection of neutrons, that usually suffers from low efficiency (as for the n-rich RIBs ^{6,8}He and ^{11}Li), or the detection of weakly bound/radioactive fragments (as for experiments involving ^{8}B or even the stable weakly bound projectiles ^{6,7}Li). Therefore, ^{7}Be represents a kind of ideal case among all light ions where the study of the reaction mechanisms at near-barrier energies can be addressed in detail.

The elastic scattering process for the ^{7}Be + ^{58}Ni system was measured at five energies around the Coulomb barrier in an experiment performed with the Twinsol [25] facility at the University of Notre Dame (USA) with a ^{8}B, ^{7}Be, ^{6}Li "cocktail" beam [21]. More recently, the fusion cross section for the same system was deduced from a measurement of the proton (evaporation) cross section at backward angles [26]. The elastic scattering angular distributions and the fusion excitation function were simultaneously fitted [27] using a theoretical approach consisting of splitting the dynamical polarization potential into two parts: the first related to the coupling between the elastic channel and the fusion process and the second corresponding to the couplings with direct reaction channels. The energy dependence of the polarization potential was found to be consistent with a "threshold anomaly" trend [28].

Near-barrier ^{7}Be scattering was also measured for very light targets such as ^{12}C [29,30] and, more recently, ^{27}Al [31] in experiments performed at the Twinsol and RIBRAS (Brazil) [32] facilities. In these cases the analysis of the energy dependence of the optical potential was subject to large uncertainties. Nonetheless, the comparison of the extracted reaction cross sections with those available for other light weakly bound (e.g., ^{9}Be, ^{6,7}Li, ^{6}He) and tightly bound (e.g., ^{16}O) projectiles interacting with ^{12}C and ^{27}Al targets showed much smaller effects related to the projectile binding energy, especially compared to reactions induced by the same projectiles on heavy (e.g., ^{208}Pb) targets. This behavior might be strongly related to the weaker Coulomb field of the carbon and aluminum targets and deserves further investigation.

Finally, Raabe and collaborators measured the fusion cross section and the yields of direct processes for the ^{7}Be + ^{238}U system at five energies around the Coulomb barrier [33]. Fusion and direct processes led to fission of the compound nucleus and the targetlike residue, respectively, and could be discriminated because in the case of direct processes (at least) an additional light charged fragment was emitted together with the fission fragments. The setup employed for the experiment had an extremely large solid angle coverage, but did not allow the unambiguous identification in mass and charge of the light fragments detected in coincidence with the fission fragments. Nevertheless, energy and Q value arguments helped the authors to infer that direct processes were essentially dominated by the ^{3}He- and ^{4}He- stripping reactions.

In the present experiment, we were able for the first time unambiguously to detect and distinguish ^{3}He and ^{4}He ions in a ^{7}Be-induced reaction, to measure their angular and energy distributions over a rather wide angular range, and to provide new insights into ^{7}Be reaction dynamics at Coulomb barrier energies.

The paper is organized as follows. Section II presents the ^{7}Be RIB production technique, while Sec. III describes the experimental setup used for the measurement. The data reduction procedure followed to extract the quasielastic differential cross section is covered in Sec. IV. Section V discusses the ^{3,4}He angular and energy distributions and their interpretation in terms of the different reaction mechanisms which can contribute to their production. Finally, some concluding remarks are given in Sec. VI.

II. SECONDARY BEAM PRODUCTION

The ^{7}Be RIB for the present experiment was produced with the EXOTIC facility [34] at the Laboratori Nazionali di Legnaro (LNL, Italy) of the Istituto Nazionale di Fisica Nucleare (INFN). The facility has been operational since 2004 and has already delivered secondary beams of ^{7}Be, ^{8}Li, ^{8}B, ^{15}O, and ^{17}F with energies in the interval 2–6 MeV/u and intensities ranging from $\sim 10^{3}$pps (for ^{8}B) to 3×10^{5} pps (for ^{7}Be, ^{8}Li, and ^{17}F).

The RIB production scheme employs two-body reactions in inverse kinematics induced by heavy-ion beams delivered by the LNL-XTU tandem Van de Graaff accelerator impinging on light gas targets. In the present experiment, the production reaction was ^{1}H(^{7}Li,^{7}Be)n (Q value = -1.97 MeV). We started from a 34.2-MeV ^{7}Li primary beam with an intensity of $\sim$70–100 pnA impinging on a $^{1}H_2$ gas target. The gas was contained in a 5-cm-long double-walled cell with 2.2-μm Havar windows. The target station was operated at a gas pressure of 1 bar and cooled to liquid nitrogen temperature (90 K) for an equivalent target thickness of about 1.35 mg/cm^2.

The ^{7}Be RIB was selected and purified from the ^{7}Li scattered beam and other contaminant beams by fine tuning the 30°-bending magnet, the 1-m-long Wien filter and the six quadrupole lenses of the EXOTIC facility. In particular, a voltage difference of $\pm$45 kV (corresponding to 90% of the maximum applicable voltage) was applied across the Wien filter electrodes.

During the secondary beam production procedure the primary beam intensity was decreased by about two orders of magnitude by inserting two 12%-transparency grids at the entrance of the tandem accelerator. In this way it was possible to monitor the RIB energy and intensity by means of a silicon surface barrier detector (active area: 300 mm^2; thickness: 300 μm) installed on the target ladder at the final

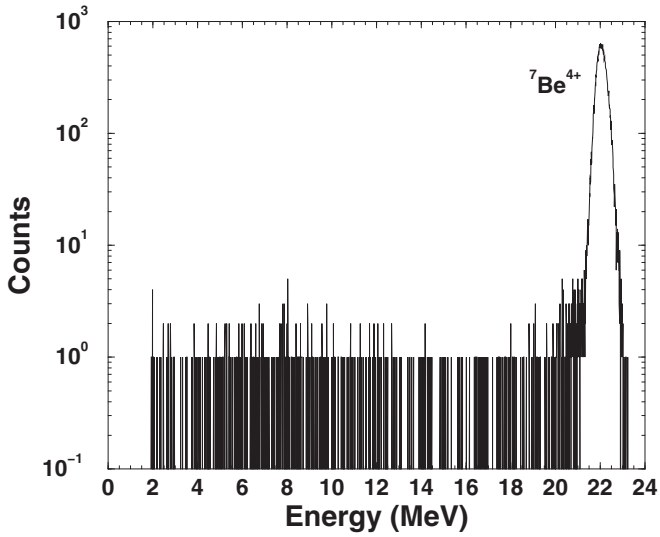

FIG. 1. Energy spectrum of the ^{7}Be secondary beam measured with a silicon detector mounted on the target ladder at the final focal plane of EXOTIC.

focal plane of EXOTIC, 8.2 m downstream of the production target. The RIB energy was subsequently crosschecked via the energy measurement of the elastic scattering events detected at the forward-most angles covered by the array employed for the experiment. Finally, the ^{7}Be RIB impinged on a 1-mg/cm^2 ^{58}Ni target with an energy of 22.0 ± 0.4 MeV, corresponding to $\sim$18% more than the nominal Coulomb barrier ($V_b = 18.6$ MeV [27] in the laboratory frame). The secondary beam intensity was typically in the range 2–3 $\times$ 10^5 pps and the beam purity was about 99%. Figure 1 shows a typical energy spectrum collected by the monitor detector located on the target ladder.

Prior to interacting with the ^{58}Ni target the ^{7}Be beam particles passed through two $x - y$ sensitive parallel plate avalanche Counters (PPACs) located along the beam line 750 mm (PPAC_A) and 214 mm (PPAC_B) upstream of the secondary target. The PPACs, described in detail in Refs. [35,36], are generally used to provide an event-by-event reconstruction of the reaction position on the target and for timing purposes. Unfortunately, in the present experiment PPAC_A, located just at the exit of the last quadrupole of EXOTIC and still crossed by high intensity marginal components of the ^{7}Li scattered beam, suffered severe radiation damage in the early stages of the experiment and worked with limited efficiency throughout the measurement. Therefore, we actively exploited only the PPAC_B signals. More precisely, the PPAC_B cathode signal was employed for the trigger logic construction, while the PPAC_B coordinate signals were utilized for on-line monitoring of the secondary beam profile (see Fig. 2 of Ref. [35] for an example).

III. EXPERIMENTAL SETUP

Charged reaction products originating from the interaction between the ^{7}Be RIB and the ^{58}Ni target were detected by means of three ΔE-$E_{\rm res}$ telescopes of the DINEX setup [37], now part of the more complex GLORIA detector array [38]. Each telescope was composed of two double-sided silicon strip detectors (DSSSDs), with thicknesses of 40–42 and 1000 μm for the ΔE and $E_{\rm res}$ layers, respectively. Each DSSSD had an active area of 50 $\times$ 50 mm^2 and the detector front and back sides were both segmented into 16 strips in order to define a pixel structure with 256 elements of $\sim$9 mm^2 area.

Two telescopes, $T1$ and $T2$, were located at forward angles and one, $T3$, at backward angles. The mean polar angles and distances from the ^{58}Ni target center were as follows: $\theta_{\rm lab} = +57.1^\circ$ and 73 mm for $T1$, $\theta_{\rm lab} = -63.5^\circ$ and 70 mm for $T2$, and $\theta_{\rm lab} = -134.2^\circ$ and 71.5 mm for $T3$. In the definition of the mean polar angles we used positive and negative values for the telescopes located in the left and right hemispheres, respectively, in a downstream view of the target plane.

The trigger of the data acquisition (DAQ) system was provided by the "AND" between the PPAC_B cathode signal and the "OR" of the signals from all the ΔE strips. A fixed-amplitude pulser signal with a rate of 2 Hz was also sent to the input of all pre-amplifiers to monitor possible amplification gain instabilities and the DAQ dead time. Trigger rates in the range 10–15 Hz were typically recorded during the experiment.

IV. QUASIELASTIC SCATTERING

Figure 2 presents a zoomed view in the region 14–21 MeV of the energy spectra collected by four groups of vertical strips of the $T1$ ΔE stage. For statistical purposes, each panel corresponds to two adjacent strips. Black histograms represent the experimental data. We clearly see that the peak

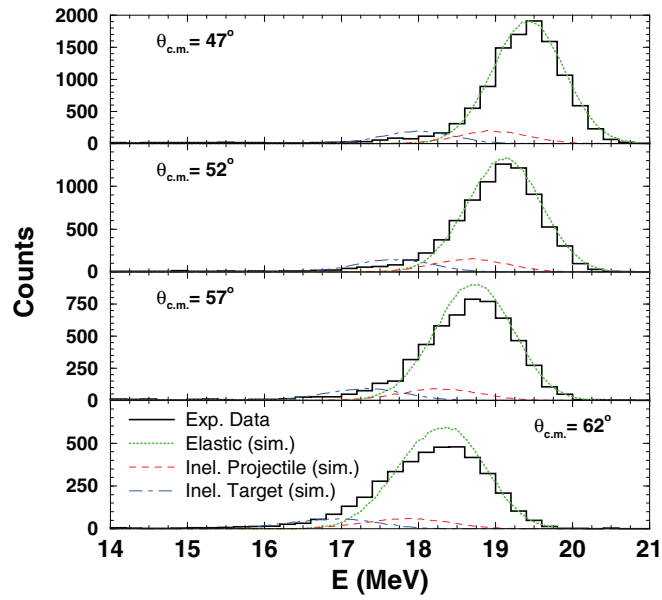

FIG. 2. (Color online) Energy spectra collected by four groups of two adjacent vertical strips of the $T1$ ΔE layer. Black histograms represent the experimental data. The lines are the results of Monte Carlo calculations (described in detail in the text) of the elastic scattering process (dotted green) and for inelastic excitations leading to the projectile (dashed red) and target (dot-dashed blue) first excited states.

located at the right-hand side of the spectra shifts towards lower energies and its integral decreases as the mean detection angle $\theta_{\text{c.m.}}$ increases. A Monte Carlo simulation was carried out to verify whether the peak evolution was consistent with the elastic scattering process. In the simulation code we took into account (i) the kinematics of the elastic scattering process; (ii) the secondary beam energy spread; (iii) the secondary beam spot on target; (iv) the geometrical displacement of the DINEX detectors around the target position; (v) the energy loss (evaluated with the code TRIM [39]) in the target thickness prior to and after the scattering process; and (vi) the detector energy resolution measured with α particles from a standard ^{241}Am source: 55–75 and 50–60 keV [FWHM (full width at half maximum)] for the ΔE and E_{res} layers, respectively. In the simulation, a random interaction position within the target thickness (1.12 μm) was assumed. Simulated events (dotted green curves in Fig. 2) were generated according to the Rutherford cross section and normalized to the experimental peak integrals at the forward-most angles ($\theta_{\text{c.m.}} \leqslant 55^\circ$), where the elastic scattering differential cross section is expected to be purely Rutherford. The agreement between experimental and simulated data is clearly evident in Fig. 2 and small deviations connected to the nuclear absorption start to manifest at about $\theta_{\text{c.m.}} = 60^\circ$.

The secondary beam energy resolution and the energy loss in the entire target thickness (about 1 MeV) could prevent the separation of pure elastic scattering events from inelastic excitations leading to the projectile and target first excited states at 0.429 and 1.454 MeV excitation energy, respectively. Therefore, Monte Carlo simulations were also carried out for these two processes and the results for the projectile and target excitations are displayed in Fig. 2 as the dashed red and dot-dashed blue lines, respectively. These two curves were arbitrarily normalized so that their integrals summed to one-tenth of the elastic peak counts in the same panel. It will be noted that events related to the projectile excitation lie completely underneath the elastic peak and that there is a substantial overlap between the energy regions for the pure elastic scattering process and the target excitation. Under these circumstances, the evaluated data have to be properly considered as "quasielastic."

Figure 3 shows the two-dimensional correlation plot of energy (E) vs detection polar angle in the laboratory frame (θ_{lab}) for charged particles releasing more than 10 MeV in the ΔE layer of telescope $T1$. Black dots correspond to the experimental data. θ_{lab} was reconstructed by uniformly randomizing the detection position within the fired pixel and assuming that the particle trajectory originated from the center of the target. The nearly empty interval at θ_{lab} slightly lower than 60° is due to a nonworking vertical strip of $T1$. Green squares and blue diamonds in Fig. 3 represent the regions where, according to the Monte Carlo simulation previously described, we expect to detect pure elastic scattering events and inelastic events leading to the target first excited state, respectively. The two regions largely overlap throughout the entire detector. However, the zone where we should observe only inelastic excitation events is only sparsely populated by the experimental data and does not significantly differ from the background region which spreads down to 10 MeV.

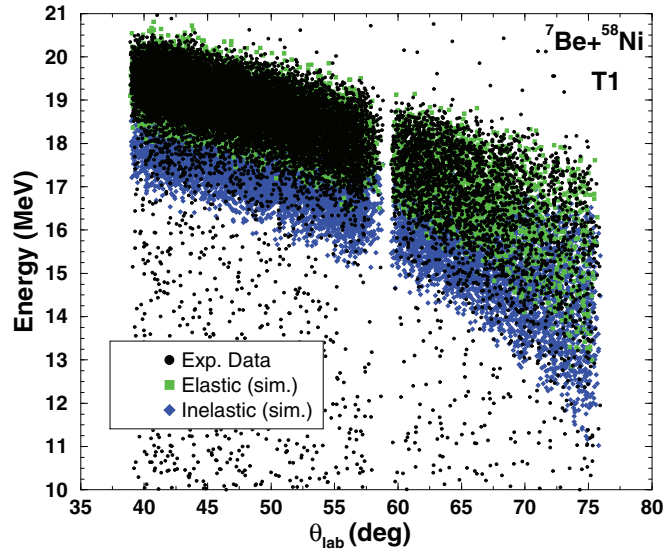

FIG. 3. (Color online) Two-dimensional correlation plot of energy (E) vs detection angle θ_{lab} for detector $T1$ located at forward angles. Experimental points are depicted as black circles. Green (light gray) squares and blue (dark gray) diamonds denote the results of Monte Carlo simulations for the elastic scattering process and inelastic excitation leading to the target first excited state at 1.454 MeV, respectively.

The situation is rather different at backward angles, as shown in Fig. 4, where the two-dimensional E vs θ_{lab} correlation plot for events releasing more than 10 MeV in the ΔE layer of telescope $T3$ is reported. In this angular range the experimental data are almost uniformly distributed over the green and blue regions and inelastic excitations may even account for one-third of the total yield of quasielastic events.

Figure 5 displays the quasielastic angular distribution for the ^{7}Be + ^{58}Ni system at a bombarding energy of 22.0 MeV.

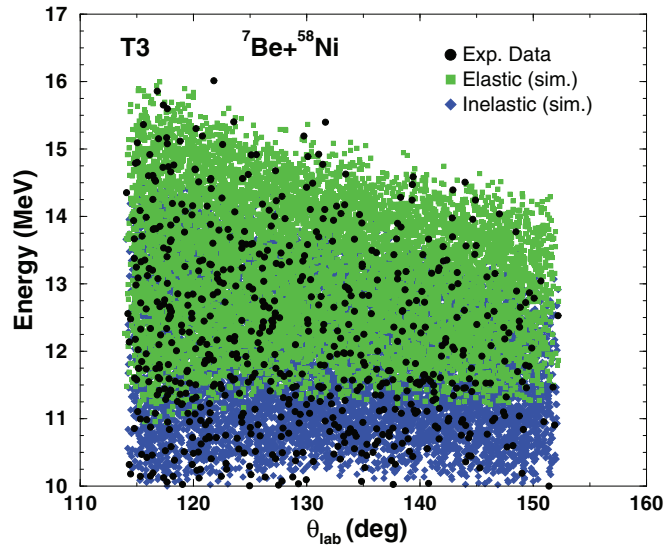

FIG. 4. (Color online) As for Fig. 3 for detector $T3$ located at backward angles.

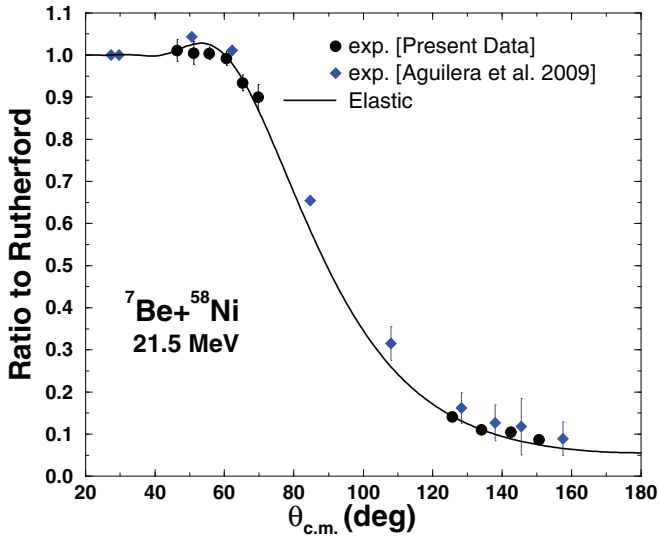

FIG. 5. (Color online) Quasielastic angular distribution for the ^{7}Be + ^{58}Ni system at 21.5 MeV. Black circles represent the present measurement, while blue diamonds are taken from an earlier measurement by Aguilera *et al.* [21]. The solid black line denotes the result of an optical model calculation using the global ^{7}Li potential parameters of Cook [41].

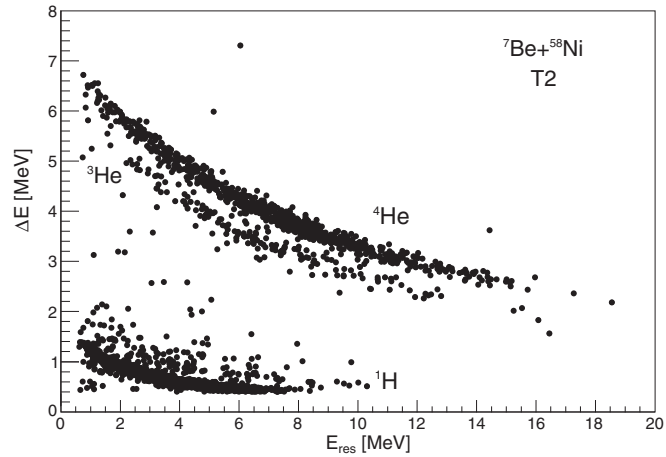

FIG. 6. ΔE-$E_{\rm res}$ correlation plot for telescope $T2$ located at forward angles.

The present evaluation (black circles in Fig. 5) was obtained by integrating the number of experimental events within the elastic/inelastic region (green and blue areas in Figs. 3 and 4) and dividing by the number of simulated data for the elastic scattering process within the same interval. To reduce statistical fluctuations, at forward (backward) angles the data from two (four) adjacent ΔE vertical strips were grouped together. Moreover, where available, the average between the evaluations provided at similar scattering angles by the telescopes located in the left ($T1$) and right ($T2$) hemispheres was considered. The resulting data were then normalized at the forward-most angles ($\theta_{\rm cm} \leqslant 55^{\circ}$), where the elastic scattering differential cross section is expected to be purely Rutherford. To account for the uncertainties in the normalization procedure, a 1.4% systematic error was added to the statistical error. The experimental points around $\theta_{\rm cm} \sim 75^{\circ}$, corresponding to the last four vertical strips of telescope $T1$, manifested some shading effects related to the thickness of the target holder (2 mm aluminum) and were therefore excluded from the plot. We note that our data compare remarkably well with the previous measurement by Aguilera *et al.* [21] (blue diamonds in Fig. 5).

Figure 5 also shows the result of an optical model calculation performed with the code FRESCO [40]. The potential parameters were obtained from the global ^{7}Li parametrization of Cook [41]. To account for the energy loss in the target thickness the calculation was performed for the beam energy at the midtarget position (21.5 MeV). The solid black line represents the calculated angular distribution for pure elastic scattering only. Test calculations established that the contribution to the quasielastic scattering from excitation of the 1.454-MeV 2^{+}_{1} state of the target may be neglected entirely, while that from the 0.429-MeV $1/2^{-}_{1}$ state of the projectile could only be distinguished at backward angles ($\theta_{\rm c.m.} > 80^{\circ}$) and the difference between quasielastic and elastic scattering was at most the same size as the experimental uncertainties. Thus the overall agreement between the experimental data and the calculation is remarkably good, considering that no parameter adjustments were made. The optical model calculation yields a total reaction cross section of 585 mb.

V. ^{3,4}He PRODUCTION

Figure 6 displays a typical ΔE-$E_{\rm res}$ correlation plot for telescope $T2$, where fairly large production yields may be observed for both ^{3}He and ^{4}He ions. Many different reaction mechanisms can lead to the presence of these two helium isotopes in the exit channel. We first list the main processes that may lead to the production of ^{3}He:

1. Exclusive breakup: ^{7}Be $\rightarrow$ ^{4}He + ^{3}He (S_{α} = 1.586 MeV);

2. ^{4}He stripping: ^{7}Be + ^{58}Ni $\rightarrow$ ^{3}He + ^{62}Zn [ground-state to ground-state Q value ($Q_{\rm gg}$) = +1.78 MeV].

The most relevant processes that may contribute to the production of ^{4}He are as follows:

1. Exclusive breakup: ^{7}Be $\rightarrow$ ^{4}He + ^{3}He (S_{α} = 1.586 MeV);

2. 1n pickup: ^{7}Be + ^{58}Ni $\rightarrow$ ^{8}Be ($\rightarrow$ ^{4}He + ^{4}He) + ^{57}Ni ($Q_{\rm gg}$ = +6.68 MeV);

3. 1n stripping: ^{7}Be + ^{58}Ni $\rightarrow$ ^{6}Be ($\rightarrow$ ^{4}He + p + p) + ^{59}Ni ($Q_{\rm gg}$ = −1.68 MeV);

4. ^{3}He stripping: ^{7}Be + ^{58}Ni $\rightarrow$ ^{4}He + ^{61}Zn ($Q_{\rm gg}$ = +9.46 MeV);

5. ^{4}He evaporation after compound-nucleus formation, i.e., complete fusion.

Figure 6 immediately shows that ^{4}He nuclei are four to five times more abundant than ^{3}He. This experimental evidence already rules out the possibility that the exclusive breakup channel dominates the reaction dynamics for the ^{7}Be + ^{58}Ni system in this energy range. If such were the case one would have expected comparable yields for the two helium isotopes.

Moreover, the exclusive breakup, $1n$-stripping and $1n$-pickup processes have in common the circumstance that they all produce (at least) two charged particles in the exit channel. On the contrary, ^{4}He stripping, ^{3}He stripping and complete fusion (the latter, according to the predictions of the statistical model code PACE2 [42] described later in the text, has an α particle evaporation multiplicity much smaller than unity) involve the detection of single reaction products only. From an experimental point of view, within the geometrical efficiency of our detector setup, we did not record any coincidence events between charged particles, neither ^{4}He + ^{3}He (a clear signature of an exclusive breakup event) nor ^{4}He + ^{1}H ($1n$ stripping) nor ^{4}He + ^{4}He ($1n$ pickup).

Therefore, we will first analyze the energy spectra and the angular distributions for ^{3}He and ^{4}He ions in terms of the processes which lead to the detection of one of the two isotopes alone. The other reaction mechanisms, for whose cross sections we will only be able to provide experimental upper limits, will be covered at the end of the section.

A. ^{3}He production

Figure 7 shows the two-dimensional correlation plot of energy vs detection angle for ^{3}He ions. We remark that the thickness of the ΔE telescope layers (40–42 μm of silicon) introduces an energy threshold in the mass and charge identification of the helium isotopes by means of the ΔE-$E_{\rm res}$ technique, since ^{3}He and ^{4}He ions with kinetic energies lower than about 6.6 and 7.3 MeV, respectively, stop completely in the first layer of the telescope.

We first made the assumption that all detected ^{3}He particles were produced by the ^{4}He-stripping process. To verify experimentally this hypothesis we performed a reaction Q value reconstruction following a procedure similar to that described in Refs. [43,44]. The Q value, defined as the difference between the kinetic energy of the final and initial states, is given by the formula

$$Q = E_{\rm He} + E_{\rm recoil} - E_{\rm beam}, \qquad (1)$$

where $E_{\rm He}$ is the ^{3}He kinetic energy, $E_{\rm beam}$ is the ^{7}Be beam energy, and $E_{\rm recoil}$ is the (undetected) recoil energy of the targetlike particle, reconstructed via linear momentum conservation. Figure 8(a) shows that the Q value spectrum has a broad distribution centered around -9.5 MeV with a FWHM of about 4 MeV. The semiclassical model of Brink for transfer processes [45] predicts an optimum Q value ($Q_{\rm opt}$) for the ^{4}He-stripping process of -8.96 MeV, rather close to that observed experimentally, especially considering that the ^{7}Be beam loses more than 1 MeV in the entire ^{58}Ni target thickness.

In addition, Fig. 8 also shows that events with reconstructed Q value less than -11 MeV were detected almost exclusively at forward angles. This circumstance is related to the fact that backward-emitted ^{3}He ions have (on average) lower kinetic energies than those produced in the forward hemisphere, thus a higher probability of stopping in the ΔE layer, and ^{3}He events with kinetic energy smaller than 6.6 MeV mostly populate the Q value region below -11 MeV.

A Monte Carlo simulation was carried out for the ^{4}He-stripping process, following the approach already described for the elastic scattering. In the calculation we assumed that the transfer process proceeded to a final state distribution of the

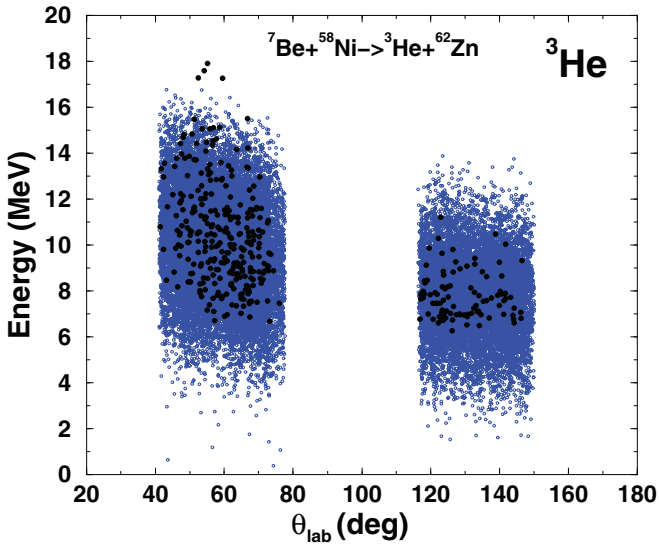

FIG. 7. (Color online) Two-dimensional correlation plot of E vs $\theta_{\rm lab}$ for ^{3}He ions. Black and blue circles represent experimental data and simulated events for the ^{4}He-stripping process, respectively. See text for additional details.

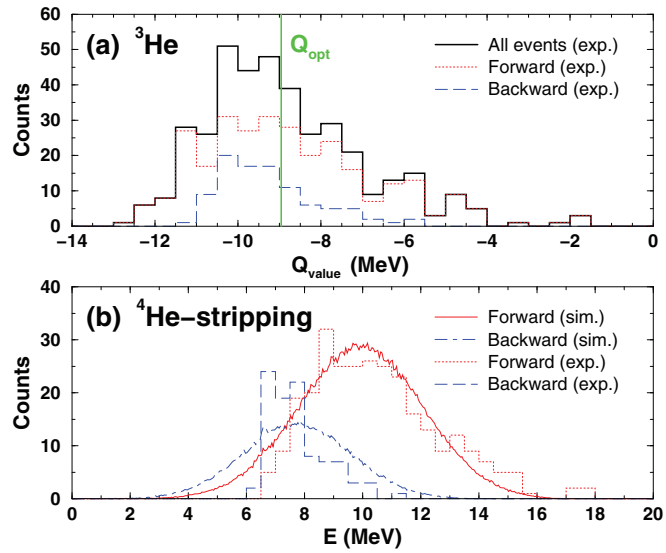

FIG. 8. (Color online) (a) Reconstructed Q value spectrum for the reaction ^{7}Be + ^{58}Ni $\rightarrow$ ^{3}He + ^{62}Zn at 22.0 MeV beam energy. The energies of the undetected ^{62}Zn ions were deduced from linear momentum conservation. The continuous black histogram represents all collected statistics, while the dotted red and dashed blue histograms correspond to events detected at forward and backward angles, respectively. The vertical green line indicates the optimum Q value calculated according to the semiclassical model of Brink [45]. (b) ^{3}He energy spectra collected by the detectors located at forward (dotted red histogram) and backward (dashed blue histogram) angles. The continuous red and the dot-dashed blue lines are the results of the Monte Carlo simulation described in the text.

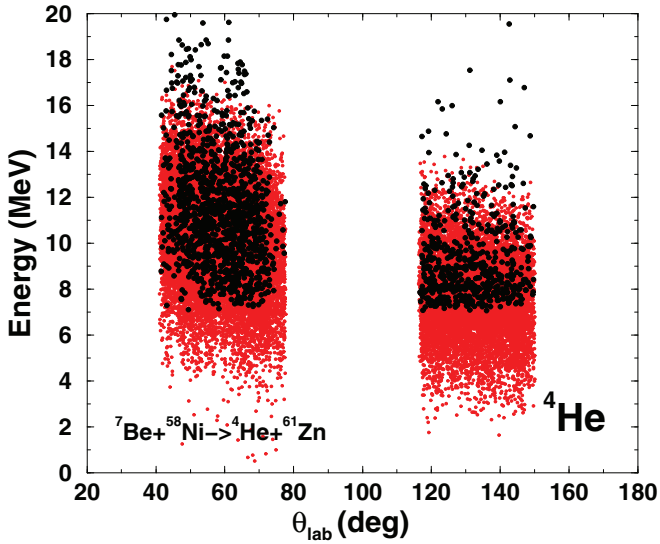

FIG. 9. (Color online) As for Fig. 7 but for the ^{4}He experimental events (black circles) and the simulated data for the ^{3}He-stripping process (red circles). Details of the calculation are given in the text.

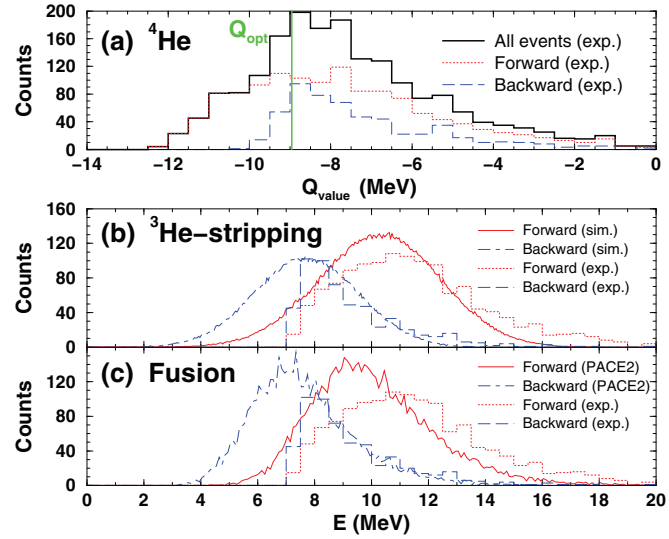

FIG. 10. (Color online) (a),(b) As in Fig. 8, but for the ^{7}Be + ^{58}Ni → ^{4}He + ^{61}Zn reaction at 22.0 MeV beam energy. (c) ^{4}He energy spectra collected by the detectors located at forward (dotted red histogram) and backward (dashed blue histogram) angles. The continuous red and the dot-dashed blue lines are the results of a PACE2 calculation of the evaporation of α particles at forward and backward angles, respectively.

targetlike particle with mean excitation energy $E_{ex}(= Q_{gg} - Q_{opt})$ of 10.7 MeV and a standard deviation of 2.0 MeV. The results of the simulation are displayed as blue dots in Fig. 7. Only four events (out of the 386 detected) exceed the energy region computed by the simulation, thus endorsing the initial assumption that ^{3}He ions might mostly originate from the ^{4}He-stripping process.

Figure 8(b) provides an additional comparison between the experimental ^{3}He energy spectra (histograms) and those obtained with the simulation (lines). Red and blue depict the spectra at forward and backward angles, respectively. The simulated data were normalized so that their integrals in the energy range above 6.6 MeV are equal to the number of experimental data. The overall trend of the data is remarkably well reproduced, especially at forward angles.

We finally employed the Monte Carlo code to estimate the fraction of ^{3}He nuclei stopped in the ΔE layer of the telescopes, crucial information to derive properly the ^{3}He angular distribution. The percentage of ^{3}He stopped increases moving towards backward angles and, according to our simulation, ranges 2–8% at forward angles and 18–24% at backward angles.

B. ^{4}He production

Figure 9 displays a correlation plot of E vs θ_{lab} for the ^{4}He ions (black dots) detected during the experiment. We again performed the Q value reconstruction procedure to establish whether the ^{4}He energy distribution was compatible with the ^{3}He-stripping process as the dominant production mechanism. The resulting Q value spectrum, shown in Fig. 10(a), is centered at ~ -8.5 MeV, somewhat greater than the predicted Q_{opt} value (-8.96 MeV) for ^{3}He stripping and significantly lower than the mean value for the reconstructed ^{3}He Q value spectrum (~ -9.5 MeV; see Fig. 8). Moreover, in contrast to the previous case, the Q value distribution for ^{4}He nuclei extends continuously almost up to 0 MeV at both forward and backward angles. We note that low energy ^{4}He events ($E \leqslant 7.3$ MeV) completely stopped in the telescope ΔE layer will contribute to the depopulation of the region below -10 MeV in the Q value spectrum, especially at backward angles.

We performed a Monte Carlo simulation for the ^{3}He-stripping process. In the calculations we considered transfer processes leading to a final state distribution of the targetlike particle with a mean excitation energy $E_{ex} = 18.4$ MeV and a standard deviation of 2.0 MeV. The results of the computation are displayed as red dots in Fig. 9 and with continuous red and dot-dashed blue lines in Fig. 10(b). The energy distribution is reasonably well reproduced, but it will immediately be seen that the experimental data extend well above the predicted region (red dots in Fig. 9), clearly suggesting that other reaction mechanisms contribute to the ^{4}He production. We first of all considered the fusion evaporation process, illustrated in the next subsection.

C. Complete fusion

We employed the code PACE2 [42], based on the statistical model, to describe α particle evaporation after formation of a compound nucleus. The fusion cross section for the ^{7}Be + ^{58}Ni system has recently been measured at 21.8 MeV bombarding energy by Martinez-Quiroz *et al.* [26]. A cross section of 394.7 ± 115.8 mb was deduced from the proton yield observed at backward angles and from the proton multiplicity (1.76) computed by PACE2. The same code predicts an α multiplicity value of 0.43, which would correspond to a cross section of approximately 170 mb.

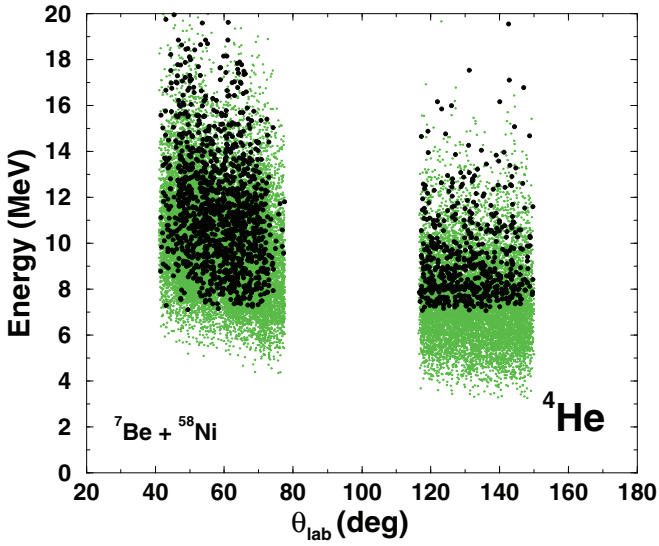

FIG. 11. (Color online) As in Fig. 9, but the simulated data were computed with the statistical model code PACE2 [42] for ^{4}He evaporation after formation of a compound nucleus (green dots). See text for additional details.

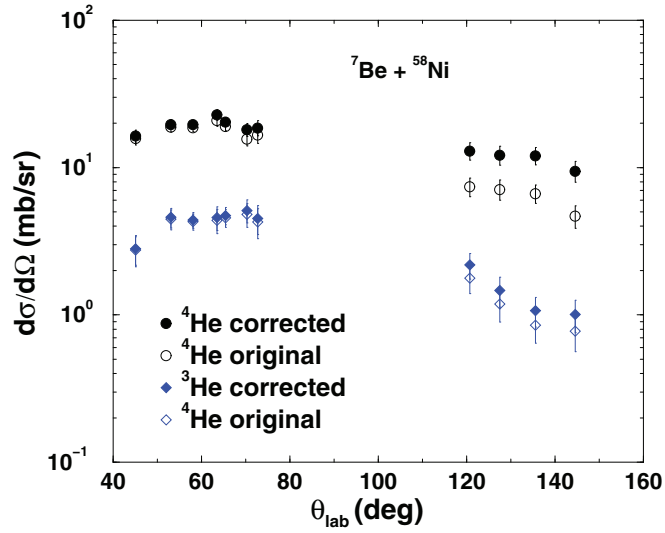

FIG. 12. (Color online) Experimental angular distributions for ^{3}He (blue diamonds) and ^{4}He (black circles) produced in the reaction ^{7}Be + ^{58}Ni at 22.0 MeV beam energy. Open and filled symbols correspond to the data evaluation before and after the correction introduced to account for the particles stopped in the ΔE layer, respectively.

The event-by-event text output file of PACE2 was used as input for a Monte Carlo simulation. All events were assumed to be generated at the midtarget position and the energy loss within the remaining target thickness was properly taken into account. The results of the simulation are displayed in Fig. 11 as green circles and in Fig. 10(c) as continuous red and dot-dashed blue lines. The evaporated α particles show a rather Maxwellian energy distribution, whose high-energy tail extends up to 18 and 15 MeV at forward and backward angles, respectively. In particular, we note that the PACE2 predictions [dot-dashed blue curve in Fig. 10(c)] nicely match the experimental energy spectrum at backward angles. On the other hand, at forward angles both fusion evaporation and ^{3}He stripping underestimate the maximum of the experimental ^{4}He energy distribution and do not account completely for the high-energy events ($E_\alpha \geqslant$ 15–16 MeV) observed at forward angles.

Thus, we can assert that both ^{3}He stripping and complete fusion contribute to the presence of ^{4}He ions in the reaction exit channel and to their single detection, but energy and Q value considerations do not help to disentangle unambiguously the individual components. However, at backward angles, ^{4}He nuclei should arise predominantly from compound-nucleus events, also taking into consideration that the reaction grazing angle for this bombarding energy is located at about $\theta_{\rm lab} = 100^\circ$ and telescope $T3$ spans approximately the angular range $\theta_{\rm lab} = [115^\circ, 150^\circ]$. In the next section we will evaluate the angular distributions of the two helium isotopes and this piece of information will then be exploited to gain additional insights into the importance of the different reaction mechanisms.

D. ^{3,4}He angular distributions

Figure 12 shows the differential cross sections for ^{3,4}He ions in the laboratory frame, with black circles and blue diamonds denoting ^{3}He and ^{4}He, respectively. Only a few counts (∼2.5% of all ^{3,4}He events) were recorded by the pixels located along the detector edges, although their overall surface corresponds to about one-fourth of the detector total active area. This occurrence might be related to the limited geometrical efficiency of the ΔE-$E_{\rm res}$ identification technique for particles impinging on the detector surface with rather tilted trajectories, i.e., close to the detector edges, with respect to ions hitting the detector surface with nearly perpendicular trajectories, i.e., in more central regions of the detector active area. For this reason the pixels along the detector edges were excluded from the evaluation procedure for the ^{3,4}He angular distributions. To reduce statistical fluctuations, data from three to four adjacent vertical strips were grouped together. The data were normalized to the number of ^{7}Be quasielastic events detected by the corresponding ΔE pixels. For the region $\theta_{\rm lab} = 70^\circ$–$75^\circ$, where some target shadow effects were observed in the evaluation of the quasielastic differential cross section, the ^{3,4}He yields were normalized to the theoretical calculation described in Sec. III (black curve in Fig. 5).

Open symbols in Fig. 12 correspond to the original data evaluation, obtained by considering the ^{3,4}He events effectively detected by means of the ΔE-$E_{\rm res}$ telescopes. However, we should also take into account events possibly stopped in the telescope ΔE layers. For this purpose we used the Monte Carlo simulations already described in the previous subsections. In particular, we assumed that ^{3}He ions entirely originated from the ^{4}He-stripping process leading to a final state distribution of the targetlike particle with a mean excitation energy $E_{\rm ex} = 10.7$ MeV and a standard deviation of 2.0 MeV. The percentage of ^{3}He ions stopped in the first layer of the telescope was estimated to be within the ranges 2–8% and 18–24% at forward and backward angels, respectively.

Filled diamonds in Fig. 12 represent the ^{3}He differential cross section after applying this correction.

The situation is slightly more complicated for ^{4}He events as they can originate from (at least) two different reaction mechanisms. We computed that for the ^{3}He stripping the percentage of ^{4}He ions stopped in the ΔE should range from 4–17% at forward angles to 41–54% at backward angles, whereas for the fusion-evaporation process we obtained the following ranges: 2–18% and 44–58% in the forward and backward hemispheres, respectively. Since the two estimates are quite similar their average values were employed for correcting the experimental data (black filled circles in Fig. 12).

E. ^{3,4}He production cross sections

The differential cross sections displayed in Fig. 12 present a gap in the angular range $\theta_{\rm lab} = [80^\circ, 115^\circ]$ since this interval was not covered by our detector setup. To provide an estimate of the ^{3,4}He total production cross sections, we tried to infer the behavior of the angular distributions in the aforementioned region by interpolating the available data sets.

Figure 13 shows the experimental ratios of the numbers of helium ions to ^{7}Be quasielastic events for the different detector regions used in the evaluation procedure of the ^{3,4}He angular distributions. Black circles and blue diamonds represent ^{4}He and ^{3}He, respectively. The two data sets exhibit a quite regular behavior, including the points around $\theta_{\rm c.m.} = 80^\circ$, where effects related to the target shadow were observed for the elastic scattering data. The dotted black and dashed blue curves in Fig. 13 correspond to interpolations of the experimental data sets for ^{4}He and ^{3}He, respectively, by means of power-law functions. The same two lines, once multiplied by the theoretical curve calculated for the elastic scattering (solid line in Fig. 5) converted to the laboratory reference frame, are displayed in Fig. 14. The agreement between the interpolated curves and the experimental ^{3,4}He angular distributions is satisfactory.

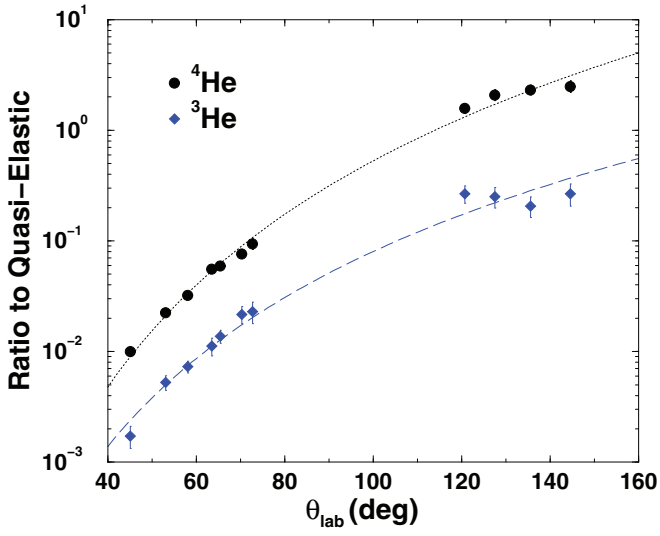

FIG. 13. (Color online) Diamonds (circles) represent the experimental ratios of ^{3}He (^{4}He) and quasielastic events for the different detector regions used in the evaluation of the angular distributions. Lines correspond to power-law interpolations of the experimental data.

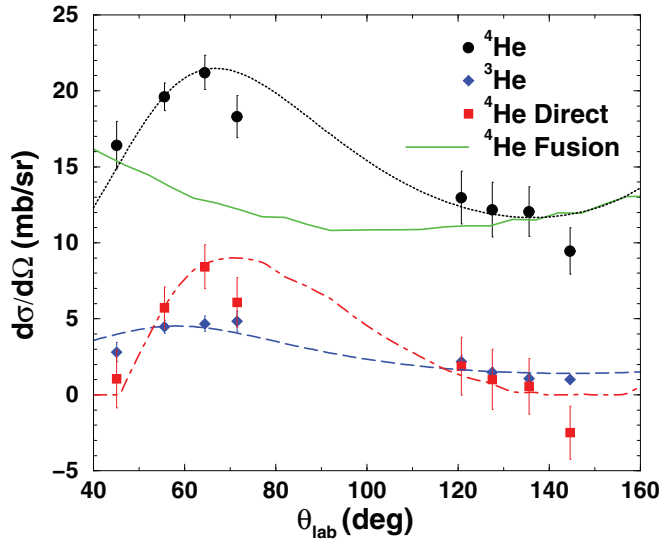

FIG. 14. (Color online) Experimental differential cross sections in the laboratory frame for ^{3}He (blue diamonds) and ^{4}He (black circles). The dashed blue and dotted black lines are the result of the interpolation of the ^{3}He and ^{4}He experimental data, respectively, according to the procedure described in the text. The solid green line is the angular distribution of evaporated α particles, computed with the code PACE2 and normalized to the data collected at backward angles. Red squares (labeled "^{4}He direct") represent the ^{4}He experimental points after subtracting the contribution from the fusion process. Finally, the dot-dashed red line is the difference between the dotted black and the solid green lines (any negative values were rounded to zero).

The angle integration of the curve derived for ^{3}He ions provides an estimate of their overall production cross section: 34.4 ± 6.3 mb. For ^{4}He, we first singled out the contribution arising from the fusion process. We used the code PACE2 to calculate the shape of the angular distribution for evaporated α particles. The curve was then normalized to the data collected at backward angles via a least-squares minimization. As already discussed, in the angular range $\theta_{\rm lab} \geqslant 115^\circ$ it is much more probable to detect ^{4}He ions produced in compound-nucleus reactions rather than in peripheral collisions. The angle-integrated cross section for evaporated α particles is 161.5 ± 11.5 mb. The corresponding α multiplicity $M_\alpha = 0.41 \pm 0.12$ is fully compatible with the predictions of PACE2 (0.43). The large error bar on the multiplicity parameter essentially reflects the uncertainty in the fusion cross section measurement [26].

Finally, we subtracted the calculated angular distribution for the fusion process from the (inclusive) ^{4}He differential cross section data to isolate the contribution from direct reaction channels and display the result in Fig. 14 as the red squares. To reduce statistical fluctuations adjacent experimental points in the angular interval $\theta_{\rm lab} = [50^\circ, 80^\circ]$ were grouped together. We applied the same subtraction procedure to the curve obtained from the interpolation of the experimental ratio

of ^{4}He ions to quasielastic events (dotted black curve in Fig. 14) and represent the result as the dot-dashed red curve in Fig. 14. The resulting curve was rounded to zero in the region $\theta_{\rm lab} \leqslant 45^\circ$, where a predominant contribution from the fusion channel is expected and no experimental measurements were carried out. The angle integration of the curve gives an overall cross section for α particles generated by direct processes of 44.1 ± 9.9 mb. In the following sections we present calculations of some of the direct reaction processes that contribute to the ^{3,4}He yields. Unfortunately, quantitative calculations for the ^{3}He and ^{4}He stripping reactions are not feasible, since they preferentially populate unbound—presumably resonant—states in the targetlike residual nuclei in excitation energy regions where little or no concrete structure information is available and none at all on the coupling strengths (i.e., the spectroscopic factors).

F. Exclusive breakup

To evaluate the contribution of the projectile breakup process to the ^{3,4}He production cross sections we performed a continuum-discretized-coupled-channel (CDCC) calculation with the code FRESCO [40]. The ^{3}He + ^{4}He cluster model of ^{7}Be employed was similar to that of Ref. [46]. Within this framework the optical potentials between the target and the individual projectile fragments and between the two fragments themselves are needed. The ^{4}He-target interaction was obtained from a Woods-Saxon potential fit to the 12-MeV ^{4}He + ^{58}Ni elastic scattering data of Ref. [47] with the following parameters: $V = 49.5$ MeV, $R_0 = 5.88$ fm, $a_0 = 0.5$ fm, $W = 11.0$ MeV, $R_W = 5.69$ fm, $a_W = 0.5$ fm. For the ^{3}He-target interaction we took the 8.95-MeV t + ^{58}Ni parameters of Ref. [48]. The internal interaction between the ^{7}Be cluster constituents was taken from [49]. This potential was properly tuned to reproduce the binding energies of the ^{7}Be ground state and first excited state and also the excitation energies of the $f_{7/2}$ ($E_{\rm ex} = 4.57$ MeV) and $f_{5/2}$ ($E_{\rm ex} = 7.21$ MeV) resonances. The continuum states in ^{7}Be were discretized into 1-MeV bins up to 12 MeV above the ^{4}He + ^{3}He breakup threshold. Finer energy bins were included for the resonances. The resulting coupled equations were integrated out to 150 fm and up to a total angular momentum $J_{\rm max} = 200$. A remarkable agreement was obtained with the experimental data for the quasielastic process, especially considering that no free parameters were employed in the computation (see Fig. 15).

Figure 16 shows that reasonable convergence was also achieved for the breakup angular distribution as soon as the maximum internal angular momentum ($\ell_{\rm max}$) of the projectile was greater than 2, thus including the $\ell = 3$ resonances. An overall breakup cross section of about 10.8 mb was obtained. A comparison with the experimental data for the production of helium isotopes shows that this process can account for about 31% and 24% of the overall ^{3}He and ^{4}He yields coming from direct processes, respectively.

Although no ^{3}He-^{4}He coincidences were detected, an upper limit for the angular distribution could still be evaluated. We used a frequentist approach based on the Neyman construction of the confidence belt [50]. The geometrical efficiency for the detection of breakup events was estimated by means of a Monte Carlo code. We carried out several simulations varying the (fixed) excitation energy ($E_{\rm ex}$) above the projectile breakup threshold in the range 0.1–8.0 MeV in 0.1 MeV steps. Since, according to the CDCC calculations, the bulk of the breakup

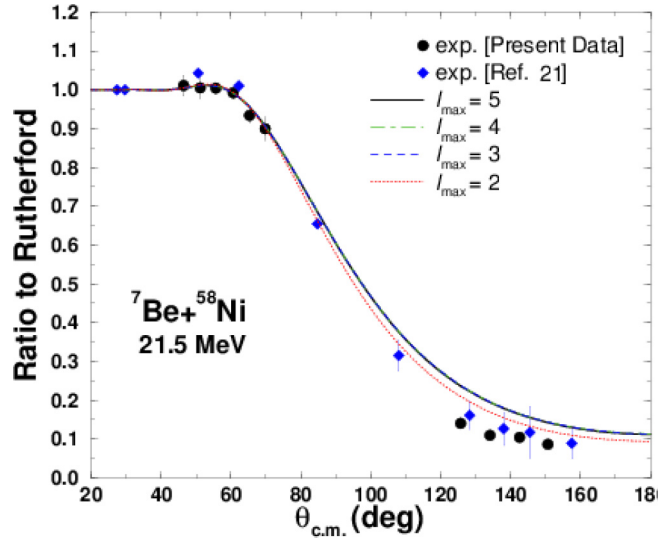

FIG. 15. (Color online) Quasielastic angular distribution for the ^{7}Be + ^{58}Ni system at 21.5 MeV beam energy. Black circles correspond to the present evaluation, while blue diamonds were taken from Ref. [21]. The dotted red, dashed blue, dot-dashed green, and continuous black lines are the results of CDCC calculations for maximum projectile internal angular momentum $\ell_{\rm max} = 2$, 3, 4, and 5, respectively.

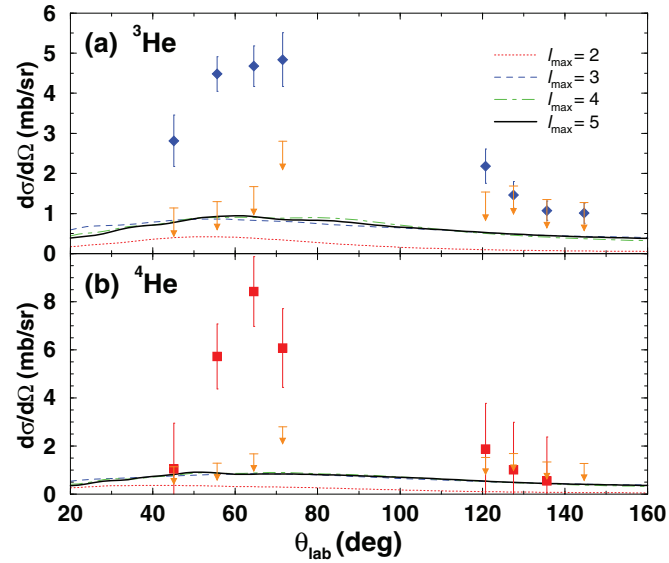

FIG. 16. (Color online) Breakup angular distributions in the laboratory frame for ^{3}He (a) and ^{4}He (b). Dotted red, dashed blue, dot-dashed green, and continuous black lines represent the differential cross sections for maximum projectile internal angular momentum $\ell_{\rm max} = 2$, 3, 4, and 5, respectively. Arrows represent the experimental upper limits (95% confidence level) for the breakup angular distributions.

excitation function should be concentrated in the excitation energy region $E_{ex} = 1.2$–2.2 MeV, we computed the average "breakup geometrical efficiency" in this energy range for each group of vertical strips used in the evaluation of the angular distribution. We obtained efficiency values of about 16% and 10% for the telescopes located at forward and backward angles, respectively. The orange arrows in Fig. 16 represent the upper limits (95% confidence level) for the exclusive breakup angular distribution. The CDCC predictions for the ^{3,4}He breakup differential cross sections are well below the experimental upper limits, thus compatible with the lack of observation of ^{3}He - ^{4}He coincidence events. We note that the increase of the upper limit values around $\theta_{lab} = 70^{\circ}$ is due to the (partial) shadow effect induced by the target holder thickness on the detectors.

Figure 17 shows that the ^{3,4}He energy distributions calculated with the CDCC formalism are rather flat and much wider than the experimental data. At forward angles, in particular, the theoretical energy distributions are peaked in the region around 8–9 MeV, i.e., about 2 MeV lower than the experimental spectra, and extend with continuity down to nearly 0 MeV, while the experimental distributions only have very small tails below 8 MeV. These outcomes strengthen the hypothesis that the breakup process does not dominate the ^{3,4}He production mechanism.

G. 1*n* pickup

The differential cross sections for the ^{7}Be + ^{58}Ni → ^{8}Be + ^{57}Ni 1*n* pickup process were calculated within the distorted-wave Born approximation (DWBA) formalism using the code FRESCO. Being a neutron transfer process, the semiclassical model of Brink predicts the preferential population of final states with $Q_{opt} \approx 0$ MeV, i.e., $E_{ex}(= Q_{gg}) = 6.68$ MeV. The calculations included 1*n*-pickup processes leading to the ^{8}Be ground state ($J^{\pi} = 0^{+}$), to its first excited state ($E_{ex} = 3.03$ MeV; $J^{\pi} = 2^{+}$) and to the four low-lying states of ^{57}Ni listed in Table I. The entrance channel optical potential was calculated using the global ^{7}Li parameters of Cook [41], already demonstrated to provide a good description of the (quasi)elastic scattering data. In default of a suitable ^{8}Be + ^{57}Ni optical potential the same parameters were used in the exit channels. The spectroscopic factors for the $\langle ^{8}\mathrm{Be}|^{7}\mathrm{Be} + n\rangle$ overlaps were taken from Cohen and Kurath [51] and the ^{7}Be + *n* binding potentials were of Woods-Saxon form with $r_0 = 1.25$ fm, $a_0 = 0.65$ fm, and a spin-orbit term of Thomas form with the same geometry and a fixed depth of 6.0 MeV; the depth of the central part was adjusted to give the correct binding energy. The spectroscopic factors and neutron binding potentials for the $\langle 58\mathrm{Ni}|^{57}\mathrm{Ni} + n\rangle$ overlaps were taken from Table I of Ref. [52], set D200E.

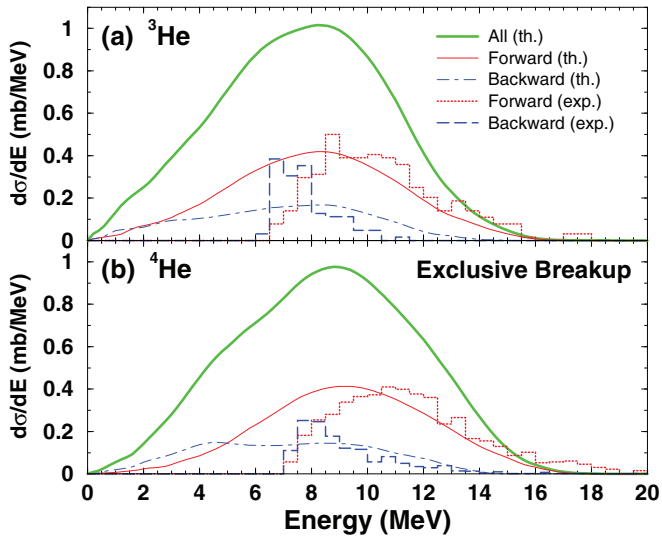

FIG. 17. (Color online) (a) ^{3}He energy spectra collected by the detectors located at forward (dotted red histogram) and backward (dashed blue histogram) angles. The thick continuous green (light gray), thin continuous red (dark gray), and dot-dashed blue lines are the CDCC predictions of the ^{3}He energy spectra for the whole angular range and for that covered by the telescopes located in the forward and backward hemisphere, respectively. The experimental data were normalized to the integrals of the theoretical curves in the energy range above 6.5 MeV. (b) Same as in (a) but for ^{4}He ions.

TABLE I. Cross sections for the individual transfer channels included in the calculations of the ^{7}Be + ^{58}Ni → ^{8}Be + ^{57}Ni 1*n*-pickup process.

^{57}Ni state	^{8}Be g.s.	^{8}Be e.s.
$E_{ex} = 0.00$ MeV; $J^{\pi} = 3/2^{-}$	0.10 mb	2.03 mb
$E_{ex} = 0.76$ MeV; $J^{\pi} = 5/2^{-}$	0.09 mb	0.47 mb
$E_{ex} = 2.57$ MeV; $J^{\pi} = 7/2^{-}$	0.30 mb	2.08 mb
$E_{ex} = 5.25$ MeV; $J^{\pi} = 7/2^{-}$	0.25 mb	0.73 mb
Total	0.74 mb	5.31 mb

The differential cross sections for the eight transfer channels considered were computed in the ^{8}Be center-of-mass reference frame, then transformed into the ^{8}Be laboratory frame. The corresponding ^{4}He angular distributions, resulting from breakup of the ^{8}Be, were evaluated with a Monte Carlo code using the ^{8}Be angular distributions as input. Figure 18(a) and Table I illustrate that the 1*n*-pickup process is essentially dominated by transfer channels leading to the ^{8}Be first excited state. The overall 1*n*-pickup differential cross section develops a slight maximum at $\theta_{lab} \approx 80^{\circ}$ and its angle integration gives a total cross section of 6.05 mb. Since each ^{8}Be breakup process produces two α particles, the DWBA calculations predict a cross section for ^{4}He ions generated from the 1*n*-pickup channel of 12.1 mb, about 27% of our estimate of the overall amount of ^{4}He produced by direct processes.

Fig. 18(a) also presents the evaluation of the experimental upper limits for the 1*n*-pickup angular distribution. The geometrical efficiency for the detection of ^{4}He - ^{4}He coincidence events was also estimated with a Monte Carlo code. We computed the efficiency value for each 1*n*-pickup channel included in the DWBA approach and then considered the weighted average, using as weights the cross sections for the individual transfer channels. Following this procedure, we obtained geometrical efficiencies in the range 15–20% for the groups of strips at forward angles and within the values

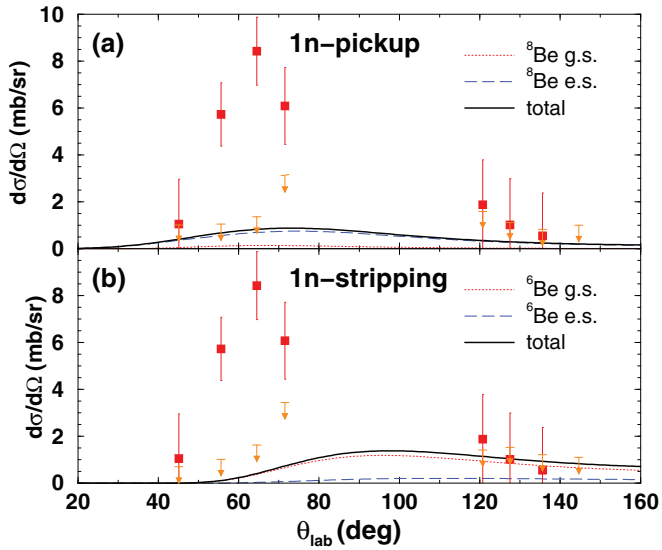

FIG. 18. (Color online) Angular distributions in the laboratory frame of ^{4}He ions produced in the 1n-pickup (a) and 1n-stripping (b) processes. Dotted red and dashed blue lines correspond to the differential cross sections for transfer processes leading to the ground and first excited states of the projectilelike fragments, respectively. The black continuous lines are the sums of the dotted red and dashed blue lines. The arrows represent the experimental upper limits (95% confidence level) for the corresponding angular distributions.

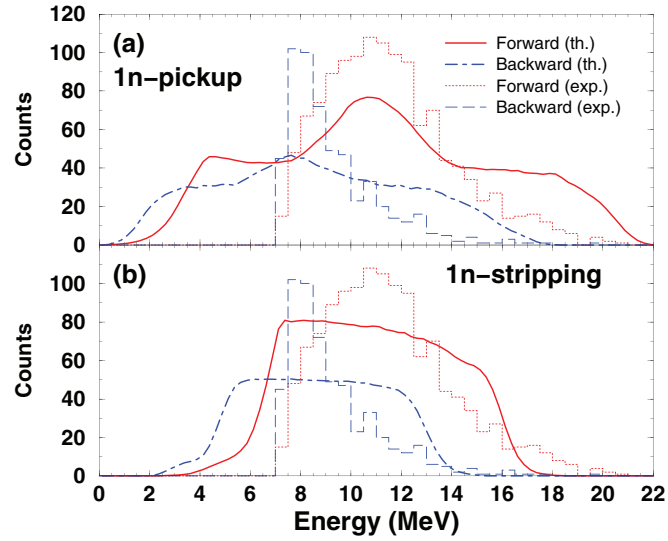

FIG. 19. (Color online) (a) Experimental ^{4}He energy spectra collected by the detectors located at forward (dotted red histogram) and backward (dashed blue histogram) angles. The continuous red and dot-dashed blue lines represent the DWBA predictions for the energy spectra of ^{4}He ions produced by the 1n-pickup process in the angular ranges covered by the telescopes located in the forward and backward hemisphere, respectively. The theoretical curves were normalized so that their integrals in the energy range above 7 MeV correspond to the number of experimental events. (b) Same as in (a) but for ^{4}He ions produced by the 1n-stripping process.

11–14% for the telescope located in the backward hemisphere. Orange arrows in Fig. 18(a) correspond to the experimental upper limits (95% confidence level) for the 1n-pickup angular distribution. The lack of experimental observation of ^{4}He - ^{4}He coincidences is consistent with the theoretical calculations and the collected statistics.

Finally, Fig. 19(a) depicts the energy distribution computed for ^{4}He ions produced after a 1n-pickup process and possibly detected by the telescopes at forward (continuous red line) or backward (dot-dashed blue line) angles. The theoretical curves were normalized so that their integrals in the energy range above 7 MeV corresponded to the number of ^{4}He experimentally detected. Both distributions show a central bump originated by the population of the ^{8}Be ground state superimposed on a much broader structure corresponding to events generated by the breakup process of ^{8}Be ions in the excited state at 3.03 MeV. A synoptic comparison of Figs. 10, 17, and 19 additionally shows that the 1n pickup could be the most relevant reaction mechanism for the production of ^{4}He ions in the energy range above 16 MeV.

H. 1*n* stripping

We finally considered the 1n-stripping process, ^{7}Be + ^{58}Ni → ^{6}Be + ^{59}Ni. For this case we also performed theoretical calculations with the code FRESCO within the DWBA formalism. According to the semiclassical model of Brink, final states corresponding to $Q_{opt} \approx 0$ MeV should be populated with the largest probability. Since Q_{gg} for the 1n-stripping process is negative, this transfer should mainly proceed through low-lying states of both the projectile- and targetlike residues. We considered 1n-stripping processes leading to the ^{6}Be ground state ($J^{\pi} = 0^{+}$), to its first excited state ($E_{ex} = 1.67$ MeV; $J^{\pi} = 2^{+}$) and to the 11 states of ^{59}Ni listed in Table II. We again used the global ^{7}Li optical model parameters of Cook [41] for both entrance and exit channels, there of course being no ^{6}Be + ^{59}Ni optical potentials available. The spectroscopic factors for the $\langle ^{7}\mathrm{Be}|^{6}\mathrm{Be} + n\rangle$ overlaps were taken from Cohen and Kurath [51] with Woods-Saxon binding potentials of the same geometry as those used

TABLE II. Cross sections for the individual transfer channels considered in the calculations for the 1n-stripping process ^{7}Be + ^{58}Ni → ^{6}Be + ^{59}Ni.

^{59}Ni state	^{6}Be g.s.	^{6}Be e.s.
$E_{ex} = 0.000$ MeV; $J^{\pi} = 3/2^{-}$	3.3955 mb	0.8588 mb
$E_{ex} = 0.339$ MeV; $J^{\pi} = 5/2^{-}$	1.8541 mb	0.2960 mb
$E_{ex} = 0.465$ MeV; $J^{\pi} = 1/2^{-}$	1.7680 mb	0.2398 mb
$E_{ex} = 0.878$ MeV; $J^{\pi} = 3/2^{-}$	0.1310 mb	0.0208 mb
$E_{ex} = 1.302$ MeV; $J^{\pi} = 1/2^{-}$	0.7575 mb	0.0618 mb
$E_{ex} = 1.680$ MeV; $J^{\pi} = 5/2^{-}$	0.1755 mb	0.0128 mb
$E_{ex} = 3.059$ MeV; $J^{\pi} = 9/2^{+}$	0.1874 mb	0.0168 mb
$E_{ex} = 4.505$ MeV; $J^{\pi} = 5/2^{+}$	0.0177 mb	0.0003 mb
$E_{ex} = 5.155$ MeV; $J^{\pi} = 1/2^{+}$	0.0012 mb	<0.0001 mb
$E_{ex} = 5.541$ MeV; $J^{\pi} = 1/2^{+}$	0.0004 mb	<0.0001 mb
$E_{ex} = 5.694$ MeV; $J^{\pi} = 1/2^{+}$	0.0003 mb	<0.0001 mb
Total	8.2886 mb	1.5072 mb

for the $\langle {}^{8}\mathrm{Be}|{}^{7}\mathrm{Be}+n\rangle$ overlaps. The spectroscopic factors and neutron binding potentials for the $\langle {}^{59}\mathrm{Ni}|{}^{58}\mathrm{Ni}+n\rangle$ overlaps were taken from Ref. [53].

Table II shows that the cross sections for the individual $1n$-stripping channels progressively decrease as the total excitation energy, defined as the sum of the ^{6}Be and ^{59}Ni excitation energies, increases, in clear agreement with the predictions of the model of Brink. Figure 18(b) displays the angular distribution in the laboratory frame for ^{4}He ions generated by the $1n$-stripping channels. For this evaluation we used the same approach as described in the previous section for the $1n$-pickup process. We first calculated the ^{6}Be angular distribution in the center-of-mass frame, then transformed the results to the laboratory frame and finally employed a Monte Carlo code to derive the differential cross section for the ^{4}He produced after the breakup of the unbound ^{6}Be nucleus. The resulting ^{4}He angular distribution is clearly dominated by stripping processes leading to the ^{6}Be ground state and develops a maximum at $\theta_{\mathrm{lab}} \cong 100^{\circ}$. The overall $1n$-stripping cross section is 9.8 mb. This value corresponds to about 22% of the cross section we estimated for the total ^{4}He production from direct processes.

Figure 18(b) also shows the experimental upper limits for the $1n$-stripping angular distribution. The plotted arrows correspond to a confidence level of 95%. The detection efficiency for ^{4}He -^{1}H coincidence events was estimated by means of a Monte Carlo simulation. We computed average geometrical efficiencies of about 16% and 20% for the two detectors located at forward angles and of about 11% for the telescope located in the backward hemisphere. Also in this case, the fact that we did not observe experimentally any ^{4}He -^{1}H coincidences is fully consistent with the theoretical predictions and the total statistics gathered during the experiment.

Finally, Fig. 19(b) displays the energy ranges foreseen at forward (continuous red line) and backward (dot-dashed blue line) angles for ^{4}He ions produced after a $1n$-stripping process. Both energy distributions present rather broad (about 9 MeV wide) single structures. This feature is clearly related to the fact that, according to the DWBA calculations, ^{4}He nuclei mostly originate from the breakup process of ^{6}Be ions produced in the ground state.

VI. CONCLUDING REMARKS

We studied the interaction of the weakly bound ^{7}Be with a ^{58}Ni target at a bombarding energy of 22 MeV. The measured quasielastic differential cross section is in very good agreement with the data from an earlier experiment and is nicely reproduced by optical model and CDCC calculations with no free parameters.

We also measured for the first time the energy and angular distributions of the two constituent clusters of ^{7}Be, ^{3}He, and ^{4}He. An investigation of the main reaction mechanisms triggering the production of the two helium isotopes faced the typical challenges currently related to studies involving RIBs: (i) low statistical accuracy and (ii) a large variety of different nuclear processes leading to the same particles in the reaction exit channel.

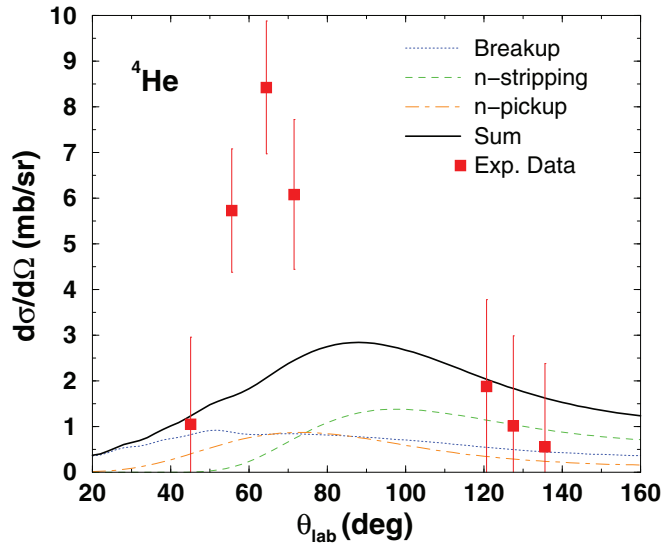

FIG. 20. (Color online) Red squares represent the experimental differential cross section for ^{4}He ions generated from direct processes in the ^{7}Be + ^{58}Ni system at 22-MeV bombarding energy. Lines correspond to the theoretical ^{4}He angular distributions calculated within the CDCC formalism for the breakup channel (dotted blue) and the DWBA approach for the $1n$-stripping (dashed green) and $1n$-pickup (dot-dashed orange) processes. The thick continuous black line is the algebraic sum of the other three theoretical curves.

The situation is essentially under control for the lighter helium isotope, as only the ^{4}He-stripping and breakup processes should contribute to the production of ^{3}He. The energy distributions at both forward and backward angles are quite consistent with a ^{4}He-stripping process as the most relevant production mechanism. According to a theoretical analysis performed within the CDCC formalism, the breakup channel should account for about 31% of the overall observed ^{3}He yield.

The question is far more complicated for the heavier helium isotope. In this case, we used the ^{4}He ions collected in the backward hemisphere (mostly originating from the fusion evaporation process) to normalize the predictions of PACE2 for the evaporated ^{4}He angular distribution. Figure 20 shows a comparison of the theoretical differential cross sections calculated for the exclusive breakup, $1n$-stripping, and $1n$-pickup processes with the experimental ^{4}He angular distribution, after the subtraction of the compound-nucleus contribution. None of the processes and not even their algebraic (i.e., no interference considered) sum can account for the large ^{4}He yield observed in the angular range $\theta_{\mathrm{lab}} = [50^{\circ}–70^{\circ}]$. Q value arguments and tentative theoretical transfer-to-continuum calculations suggest that this extra yield might be due to the ^{3}He-stripping process. According to the analysis performed within the DWBA and CDCC formalisms, the exclusive breakup, $1n$-pickup, and $1n$-stripping processes contribute about 24%, 27%, and 22 %, respectively, to the overall amount of ^{4}He produced by direct processes, thus leaving the remaining 26% to the ^{3}He-stripping channel.

In conclusion, our experiment provides the first very interesting insights into the reaction dynamics of the weakly

bound ^{7}Be RIB incident on a ^{58}Ni target at Coulomb barrier energies. Further studies are needed to disentangle completely the several reaction mechanisms producing ^{3}He and ^{4}He ions in the reaction exit channels. Future experiments should mainly aim at (i) improving the statistical accuracy of the collected data, (ii) ensuring a larger solid angle coverage, and (iii) increasing the geometrical efficiency for the detection of coincidence events. From a theoretical point of view extension of the CDCC formalism consistently to include transfer-to-continuum channels would be of great help to corroborate the interpretation of the experimental results.

ACKNOWLEDGMENTS

This work was partially supported by the Italian Minister for Education, University and Research (MIUR) within Project No. RBFR08P1W2_001 (FIRB 2008) and the National Science Centre of Poland under Contract No.UMO-2014/14/M/ST2/00738 (COPIN-INFN Collaboration). The research leading to these results has also received funding from the European Commission, Seventh Framework Programme (FP7/2007-2013) under Grant Agreement No. 600376.

[1] L. F. Canto, P. R. S. Gomes, R. Donangelo, and M. S. Hussein, Phys. Rep. **424**, 1 (2006).
[2] J. F. Liang and C. Signorini, Int. J. Mod. Phys. E **14**, 1121 (2005).
[3] N. Keeley, R. Raabe, N. Alamanos, and J. L. Sida, Prog. Part. Nucl. Phys. **59**, 579 (2007).
[4] N. Keeley, N. Alamanos, K. W. Kemper, and K. Rusek, Prog. Part. Nucl. Phys. **63**, 396 (2009).
[5] M. Mazzocco, Int. J. Mod. Phys. E **19**, 977 (2010).
[6] N. Keeley, K. W. Kemper, and K. Rusek, Eur. Phys. J. A **50**, 145 (2014).
[7] P. R. S. Gomes, J. Lubian, I. Padron, and R. M. Anjos, Phys. Rev. C **71**, 017601 (2005).
[8] J. M. B. Shorto, P. R. S. Gomes, J. Lubian, L. F. Canto, S. Mukherjee, and L. C. Chamon, Phys. Lett. B **678**, 77 (2009).
[9] E. F. Aguilera, I. Martel, A. M. Sanchez-Benitez, and L. Acosta, Phys. Rev. C **83**, 021601(R) (2011).
[10] A. Di Pietro *et al.*, Phys. Rev. C **69**, 044613 (2004).
[11] A. Navin *et al.*, Phys. Rev. C **70**, 044601 (2004).
[12] A. Chatterjee *et al.*, Phys. Rev. Lett. **101**, 032701 (2008).
[13] D. Escrig *et al.*, Nucl. Phys. A **792**, 2 (2007).
[14] L. Acosta *et al.*, Phys. Rev. C **84**, 044604 (2011).
[15] J. P. Bychowski, P. A. DeYoung, B. B. Hilldore, J. D. Hinnefeld, A. Vida, F. D. Becchetti, J. Lupton, T. W. O'Donnell, J. J. Kolata, G. Rogachev, and M. Hencheck, Phys. Lett. B **596**, 26 (2004).
[16] P. A. De Young *et al.*, Phys. Rev. C **71**, 051601(R) (2005).
[17] J. J. Kolata *et al.*, Phys. Rev. C **75**, 031302(R) (2007).
[18] R. Raabe *et al.*, Nature (London) **431**, 823 (2004).
[19] A. Lemasson *et al.*, Phys. Rev. Lett. **103**, 232701 (2009).
[20] A. Lemasson *et al.*, Phys. Rev. C **82**, 044617 (2010).
[21] E. F. Aguilera *et al.*, Phys. Rev. C. **79**, 021601(R) (2009).
[22] E. F. Aguilera *et al.*, Phys. Rev. Lett. **107**, 092701 (2011).
[23] M. Cubero *et al.*, Phys. Rev. Lett. **109**, 262701 (2012).
[24] J. P. Fernandez-Garcia *et al.*, Phys. Rev. Lett. **110**, 142701 (2013).
[25] F. D. Becchetti, M. Y. Lee, T. W. O'Donnell, D. A. Roberts, J. J. Kolata, L. O. Lamm, G. Rogachev, V. Guimarães, P. A. De Young, and S. Vincent, Nucl. Instrum. Methods Phys. Res., Sect. A **505**, 377 (2003).
[26] E. Martinez-Quiroz *et al.*, Phys. Rev. C **90**, 014616 (2014).
[27] A. Gomez Camacho, and E. F. Aguilera, Phys. Rev. C **90**, 064607 (2014).
[28] G. R. Satchler, Phys. Rep. **199**, 147 (1991).
[29] A. Barioni, J. C. Zamora, V. Guimarães, B. Paes, J. Lubian, E. F. Aguilera, J. J. Kolata, A. L. Roberts, F. D. Becchetti, A. Villano, M. Ojaruega, and H. Jiang, Phys. Rev. C **84**, 014603 (2011).
[30] J. C. Zamora *et al.*, Phys. Rev. C **84**, 034611 (2011).
[31] V. Morcelle *et al.*, Phys. Rev. C **89**, 044611 (2014).
[32] R. Lichtenthäler *et al.*, Eur. Phys. J. A **25**, s733 (2005).
[33] R. Raabe, C. Angulo, J. L. Charvet, C. Jouanne, L. Nalpas, P. Figuera, D. Pierroutsakou, M. Romoli, and J. L. Sida, Phys. Rev. C **74**, 044606 (2006).
[34] F. Farinon *et al.*, Nucl. Instrum. Methods Phys. Res., Sect. B **266**, 4097 (2008).
[35] M. Mazzocco *et al.*, Nucl. Instrum. Methods Phys. Res., Sect. B **317**, 223 (2013).
[36] M. Mazzocco *et al.*, Phys. Rev. C **82**, 054604 (2010).
[37] N. Patronis *et al.*, Phys. Rev. C **85**, 024609 (2012).
[38] G. Marquínez-Durán, L. Acosta, R. Berjillos, J. A. Dueñas, J. A. Labrador, K. Rusek, A. M. Sánchez-Benítez, and I. Martel, Nucl. Instrum. Methods Phys. Res., Sect. A **755**, 69 (2014).
[39] J. F. Ziegler *et al.*, *The Stopping and Range of Ions in Solids* (Pergamon, Oxford, 1984), Vol. 1.
[40] I. J. Thompson, Comput. Phys. Rep. **2**, 167 (1988).
[41] J. Cook, Nucl. Phys. A **388**, 153 (1982).
[42] A. Gavron, Phys. Rev. C **21**, 230 (1980).
[43] R. Rafiei, R. du Rietz, D. H. Luong, D. J. Hinde, M. Dasgupta, M. Evers, and A. Diaz-Torres, Phys. Rev. C **81**, 024601 (2010).
[44] D. H. Luong, M. Dasgupta, D. J. Hinde, R. du Rietz, R. Rafiei, C. J. Lin, M. Evers, and A. Diaz-Torres, Phys. Rev. C **88**, 034609 (2013).
[45] D. M. Brink, Phys. Lett. B **40**, 37 (1972).
[46] N. Keeley, K. W. Kemper, and K. Rusek, Phys. Rev. C **66**, 044605 (2002).
[47] L. L. Lee, Jr. and J. P. Schiffer, Phys. Rev. **134**, B765 (1964).
[48] D. Fick, R. E. Brown, W. Grüebler, R. A. Hardekopf, and J. S. Hanspal, Phys. Rev. C **29**, 324 (1984).
[49] B. Buck and A. C. Merchant, J. Phys. G **14**, L211 (1988).
[50] G. J. Feldman and R. D. Cousins, Phys. Rev. D **57**, 3873 (1998).
[51] S. Cohen and D. Kurath, Nucl. Phys. A **101**, 1 (1967).
[52] J. Van de Wiele, H. Langevin-Joliot, F. Jourdan, J. Guillot, E. Gerlic, L. H. Rosier, A. Willis, C. Djalali, M. Morlet, E. Tomasi-Gustafsson, N. Blasi, S. Micheletti, and S. Y. van der Werf, Phys. Rev. C **50**, 2935 (1994).
[53] O. Iwamoto, A. Nohtomi, Y. Uozumi, T. Sakae, M. Matoba, M. Nakano, T. Maki, and N. Koori, Nucl. Phys. A **576**, 387 (1994).